THE ASTROPHYSICAL JOURNAL, 526:976–990, 1999 December 1

THE EFFECT OF CRYSTALLIZATION ON THE PULSATIONS OF WHITE DWARF STARS

M. H. MONTGOMERY[1,2] AND D. E. WINGET[1]
Received 1999 May 11; accepted 1999 July 16

ABSTRACT

We consider the pulsational properties of white dwarf star models with temperatures appropriate for the ZZ Ceti instability strip and with masses large enough that they should be substantially crystallized. Our work is motivated by the existence of a potentially crystallized DA variable (DAV), BPM 37093, and the expectation that digital surveys in progress will yield many more such massive pulsators. A crystallized core makes possible a new class of oscillations, the torsional modes, although we expect these modes to couple at most weakly to any motions in the fluid and therefore to remain unobservable. The *p*-modes should be affected at the level of a few percent in period, but are unlikely to be present with observable amplitudes in crystallizing white dwarfs any more than they are in the other ZZ Ceti's. Most relevant to the observed light variations in white dwarfs are the *g*-modes. We find that the kinetic energy of these modes is effectively excluded from the crystallized cores of our models. As increasing crystallization pushes these modes farther out from the center, the mean period spacing $\langle \Delta P \rangle$ between radial overtones increases substantially with the crystallized mass fraction, $M_{\rm cr}/M_*$. In addition, the degree and structure of mode trapping is affected. The fact that some periods are strongly affected by changes in the crystallized mass fraction while others are not suggests that we may be able to disentangle the effects of crystallization from those due to different surface layer masses.

Subject headings: dense matter — stars: evolution — stars: oscillations — white dwarfs

1. ASTROPHYSICAL CONTEXT

The theoretical study of pulsating crystalline objects extends many years into the past. One of the first numerical studies was by Alterman, Jarosch, & Pekeris (1959), who modeled global oscillations of the Earth. Their main interest was in fitting the oscillation period of 57 minutes that was excited by the Kamchatka earthquake of 1952. In the process, they examined how the central density in their models allowed them to match the periods of other oscillation modes that were also observed to be excited by the earthquake.

In an astrophysical context, Hansen & Van Horn (1979) treated oscillations in white dwarf models with a crystalline inner core. Since it was known that 1 $M_\odot$ models with $T_{\rm eff} \sim 10{,}000$ K were in the process of crystallizing (Lamb & Van Horn 1975; Van Horn & Savedoff 1976), Hansen & Van Horn self-consistently treated the response of the crystalline core to the pulsations. Their main interest was in explaining the observed period ranges of the ZZ Ceti's in terms of low radial order oscillations. They found that the *g*-mode periods were decreased by the presence of crystallization, contrary to our present findings.

McDermott, Van Horn, & Hansen (1988) treated oscillations in neutron star models with a fluid core, a solid crust, and a thin surface fluid "ocean." They considered neutron star oscillations as a possible explanation for the observed irregularities in the timing of subpulses from radio pulsars, and as a source of the observed periodicities in many X-ray burst sources. They found *g*-modes that were trapped in the cores of their models, as well as those that were trapped in the surface oceans.

Finally, Bildsten & Cutler (1995) considered *g*-mode oscillations in the thin surface oceans of accreting neutron star models. Their aim was to explain the observed 5–7 Hz quasi-periodic oscillations in the brightest accreting neutron star systems. They found a good match to these frequencies for low order, $l = 1$ *g*-modes.

Why, then, does this problem need to be reexamined in the context of white dwarf stars? As is often the case, new observations and new circumstances have again made this problem one worth considering, but in more detail than the general analyses of the past. For example, the pioneering calculations of Hansen & Van Horn (1979) were focused primarily on the range of normal mode periods that are possible given a crystallized core, not with the details of how the periods of high-overtone *g*-modes are affected at the level of 5%–10%. At the time, there were no known high-mass white dwarf pulsators, and precise mode identifications for *any* pulsating white dwarf had yet to be attempted.

That situation changed with the discovery of pulsations in BPM 37093 (Kanaan et al. 1992), a high-mass ZZ Ceti star (see Fig. 1) that should be substantially crystallized (Winget et al. 1997); depending on the C/O ratio in its core, it should be between 50% and 90% crystallized by mass. Depending on the details of its nuclear history, its core could be composed of even heavier elements, such as Ne (Iben 1991), which would imply that it is more than 90% crystallized (Winget et al. 1997). The Whole Earth Telescope (WET) examined this target in the spring of 1998 and found at least eight independent frequencies, three of which had been previously seen by Kanaan (1996). Thus, the potential to perform asteroseismology on this object requires us to make a more detailed theoretical investigation of the properties of crystallized pulsators.

One hope is that we will be able to independently determine the crystallized mass fraction, $M_{\rm cr}/M_*$, and thereby provide a direct test of the theory of crystallization, now nearly four decades old (Abrikosov 1960; Kirzhnits 1960; Salpeter 1961). This subject is relevant to the astronomical community at large, since phase separation of C and O during crystallization, and, indeed, crystallization itself, rep-

[1] McDonald Observatory and Department of Astronomy, The University of Texas at Austin, Austin, TX 78712.
[2] Institut für Astronomie, Universität Wien, Türkenschanzstraße 17, A-1180 Wien, Austria.

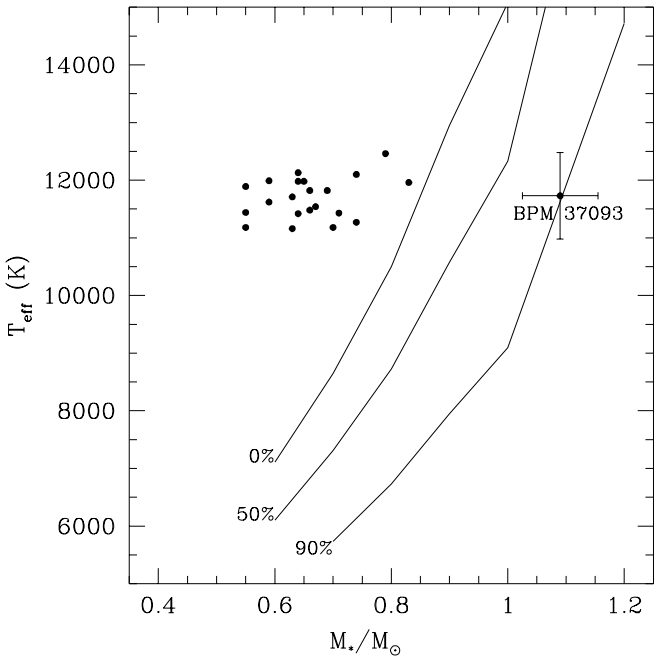

FIG. 1.—Position of BPM 37093 relative to the other ZZ Ceti's in Bergeron et al. (1995) as a function of $T_{\rm eff}$ and $M_*/M_\odot$. The lines correspond to constant amounts of crystallized mass fraction, assuming a pure oxygen core. If BPM 37093 has an oxygen core, it should be ~90% crystallized, and for a carbon core, ~50% crystallized.

resent the largest sources of systematic uncertainties in the age of the local Galactic disk as derived from the white dwarf luminosity function. In addition, understanding the internal structure of white dwarfs may prove vital in fitting cosmological models to supernova Ia (SN Ia) data (Garnavich et al. 1998), so that systematic differences in the absolute magnitudes of the SNe Ia can be corrected for the evolutionary differences in the SN progenitors (Höflich, Wheeler, & Thielemann 1998).

Finally, digital surveys now in progress promise to add considerably to the presently known number of cool white dwarfs. For instance, the Sloan Digital Sky Survey (Gunn 1995) should increase this number by a factor of approximately 20, with the result that we may have 20 such stars with which to test the theory of crystallization.

2. EVOLUTIONARY MODELS

The basis for our equilibrium models is an updated version of WDEC, the White Dwarf Evolutionary Code, as described in Lamb & Van Horn (1975) and Wood (1990, 1992). Here we present only a brief summary of the input physics in our models, with references provided for a more complete description.

In the cores of our models we use the Lamb equation of state (EOS; Lamb 1974), and in the envelopes we use the tabular EOS of Fontaine, Graboske, & Van Horn (1977). We employ the additive volume technique to interpolate between pure compositions for the carbon/oxygen mixture in the core and the hydrogen/helium/carbon mixture in the envelope. The chemical profiles of the composition transition zones in the envelope are treated with an adaptation of the method of Arcoragi & Fontaine (1980). Essentially, these profiles mimic those that would be obtained in diffusive equilibrium, but contain additional parameters controlling the thickness of the transition regions (Bradley, Winget, & Wood 1993).

The question of crystallization and our treatment of it is central to our analysis. For a model with a given mass, $T_{\rm eff}$, and composition, the Lamb EOS does return a unique answer for the degree of crystallization; the critical value of Γ is given by $\Gamma_{\rm cr} \simeq 160$, where $\Gamma \equiv Z^2e^2/\langle r\rangle k_{\rm B} T$ is the ratio of Coulomb energy between neighboring ions to each ion's kinetic energy. More recent calculations indicate a somewhat higher value for this ratio, $\Gamma_{\rm cr} \simeq 180$ (Ogata & Ichimaru 1987). Our approach is to compute equilibrium models using WDEC and the Lamb EOS, which results in models with a self-consistently computed value of the crystallized mass fraction. When we perform a pulsational analysis of these models, however, we take the crystallized mass fraction to be a free parameter, in hopes of using asteroseismology to place constraints on the degree of crystallization. The underlying assumption here is that two equilibrium models that differ only in the degree of crystallization have virtually identical pressure, density, and temperature profiles.

While this is not a physically self-consistent procedure, it is justifiable for two reasons. First, the main physical effect of crystallization is the release of latent heat; this provides the models with an additional energy source, which means that at a given $T_{\rm eff}$ they are older. This clearly has no effect on the pulsational properties, which depend only on the structural parameters of a given equilibrium model. Second, the density change at crystallization is quite small, $\delta\rho/\rho \sim 10^{-3}$ (Lamb & Van Horn 1975), so the difference in, for example, $\rho(r)$, $P(r)$, and $T(r)$ between two models that differ only in the amount of crystallization is accordingly quite small. As we show in § 5.2, the effect of crystallization upon g-mode pulsations can be accurately taken into account through a modified boundary condition at the assumed solid/fluid interface.

3. ASYMPTOTIC NONRADIAL OSCILLATION THEORY

Stars that are fluid (uncrystallized) can undergo nonradial motions, which have been labeled g- and p-mode oscillations. In the linear limit, these modes of oscillation are spheroidal, with the Eulerian perturbations of variables such as the density and pressure having the angular spatial dependence of a single spherical harmonic [i.e., ρ', $p' \propto Y_l^m(\theta, \phi)$]. From a local analysis, the radial wavenumber k_r is given by

$$k_r^2 = \frac{1}{\sigma^2 c_s^2}(\sigma^2 - L_l^2)(\sigma^2 - N^2)\,, \qquad (1)$$

where σ is the angular frequency of the mode, c_s is the sound speed, $L_l^2 \equiv l(l+1)c_s^2/r^2$ is the square of the Lamb/acoustic frequency, r is the radial variable, and N^2 is the famed Brunt-Väisälä frequency (see Unno et al. 1989 for a more complete discussion). From equation (1), we see that a mode is propagating in a region (i.e., has $k_r^2 \geq 0$) if $\sigma^2 > L_l^2, N^2$, *or* $\sigma^2 < L_l^2, N^2$. Thus, the modes separate cleanly into two classes:

1. *p-modes*: $\sigma^2 > L_l^2, N^2$ is the "high-frequency limit," $\sigma_k \sim k\pi/(\int_{r_1}^{r_2} dr/c_s)$, and displacements becoming vertical near the surface.

2. *g-modes*: $\sigma^2 < L_l^2, N^2$ is the "low-frequency limit," with $P_k \sim (2\pi^2 k)/[l(l+1)]^{1/2}(\int_{r_1}^{r_2} N\,dr/r)^{-1}$, and displacements becoming horizontal near the surface.

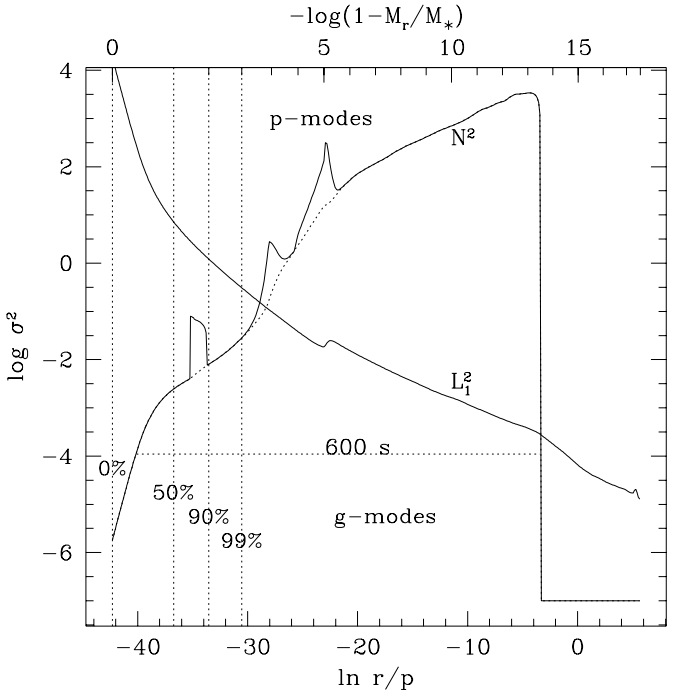

FIG. 2.—Propagation diagram showing N^2 and L_1^2 as a function of ln (r/p) (*bottom axis*) and $-\log(1 - M_r/M_*)$ (*top axis*); the center is on the left and the surface is on the right. The region of propagation of a 600 s g-mode is shown. The vertical dashed lines are labeled by the percentage of mass interior to these regions, i.e., the 90% line indicates the boundary at which 90% of the mass of the model is inside this point. We see that a model that is this crystallized now has an inner turning point for g-mode propagation considerably farther out than in the uncrystallized case.

Here r_1 and r_2 are the inner and outer classical turning points, respectively, at which $k_r = 0$ for a given σ. We see that in the asymptotic limit, the p-modes are uniformly spaced in frequency as a function of radial order k, while the g-modes are uniformly spaced in period.

A useful diagnostic for the frequency spectrum of a given white dwarf model is the propagation diagram, an example of which is shown in Figure 2, where we have labeled the high- and low-frequency domains of the p- and g-modes; the model is of a 1.1 $M_\odot$ white dwarf with $T_{\rm eff} = 12{,}200$ K. The horizontal axis is given in terms of the radial variable ln (r/p), which is the natural logarithm of the radius divided by the pressure, where both r and p are given in cgs units. This radial variable has the desirable property that it increases monotonically outward from the center and provides increased resolution in both the core (where r approaches zero) and the envelope (where p approaches zero). Along the upper axis, we display the more commonly used radial variable $-\log(1 - M_r/M_*)$, which may be more easily related to the structural parameters of the models.

We note that the bumps in N^2 and L_l^2 correspond to the C/O, He/C, and H/He transition zones. For instance, using the upper axis to obtain estimates of $-\log(1 - M_r/M_*)$, we see that the outer two transition zones have $M_{\rm H}/M_* \sim 10^{-5}$ and $M_{\rm He}/M_* \sim 10^{-3}$, which are in fact the values assumed in these models.

4. THE EFFECT OF A CRYSTALLINE CORE

How does a crystalline core affect the oscillations of a star? As we introduce a solid core into our models, two things occur: (1) a new class of modes appears (the torsional/toroidal modes, in this case), and (2) the preexisting p- and g-modes are modified. We now treat these cases separately.

4.1. *Torsional Modes*

The torsional modes, or t-modes, are very special nonradial modes, characterized by zero radial displacement and zero compression, i.e., ξ_r and $\nabla \cdot \boldsymbol{\xi}$ both vanish, where $\boldsymbol{\xi}$ is the displacement vector. The dispersion relation for these modes is

$$k_r^2 = \frac{1}{v_s^2}(\sigma^2 - T_l^2)\,, \tag{2}$$

where $v_s^2 = \mu/\rho$ is the square of the shear velocity, μ is the shear modulus, and $T_l^2 = [l(l+1) - 2]v_s^2$ is the "torsional frequency." They propagate in the region defined by $\sigma^2 > T_l^2$, and their frequency spectrum is equally spaced, as is the case with p-modes, with

$$\sigma_k \sim \frac{k\pi}{\int dr/v_s}\,.$$

As we might expect, the $k = 1$ period for these modes goes as R_*/v_s, the crossing time for a shear wave.

In Figure 3, we show a propagation diagram for t-modes with $l = 2$, using the same white dwarf model as in Figure 2. If we imagine a model that is 90% crystallized, then the t-mode can potentially propagate anywhere inside the 90% mass point in the model. If the mode is an $l = 2$ mode, then its region of propagation is restricted further, to the region for which its frequency is greater than the torsional frequency, i.e., $\sigma^2 > T_2^2$. For a 1 s mode, this corresponds to the part of the horizontal dotted line that lies to the left of

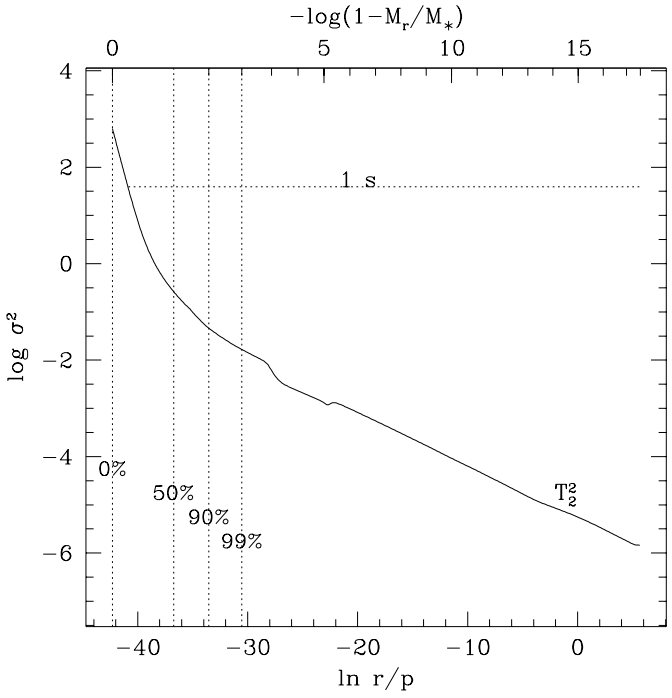

FIG. 3.—Propagation diagram for t-modes for $l = 2$. The t-modes propagate only in the crystallized region, e.g., only to the left of the 90% crystallized line for a 90% crystallized model. We note that for $l = 1$, we have $T_1^2 = 0$, so the modes propagate throughout the entire crystallized region in this case.

the 90% point in Figure 3. We note that for all the $l = 1$ modes, we have $T_1^2 = 0$, so these modes propagate throughout the entire crystallized region.

Observable consequences of the t-modes, if any exist, are difficult to identify. The longest period t-modes should have periods of ~ 20 s, which is too short to explain the observed oscillations in the ZZ Cetis of 100s of seconds.[3] In addition, these modes should not be able to couple (in the linear limit) to the fluid at the solid/fluid interface, so these oscillations should be unable to propagate from the crystalline core through the fluid to the surface. In addition, the different angular structure of the t-modes should make any nonlinear coupling between these modes and the ordinary p- and g-modes very weak; to the first nonlinear order this coupling will be zero. As a result, we expect these modes to be unobservable unless crystallization has proceeded out into the photosphere. The oldest known white dwarfs in the Galaxy are not yet cool enough for this to have occurred. We therefore turn our attention to the p- and g-modes.

4.2. *Spheroidal Modes*

4.2.1. *p-Modes*

For pressure waves traveling in a solid medium, the velocity, v_p, is given by

$$v_p^2 = \frac{\lambda + 2\mu}{\rho} ,$$

where $\lambda = \Gamma_1 P - 2\mu/3$, ρ and P are the density and pressure, respectively, and Γ_1 is the usual adiabatic exponent (Landau & Lifshitz 1975). If we treat the nonzero μ as a perturbation, we find that

$$\frac{\delta v_p}{v_p} \sim \frac{2\mu}{3\Gamma_1 P} ,$$

where δv_p is the change in v_p due to the finite shear modulus. In the cores of our 1.1 $M_\odot$ models, we typically find $\mu/p \sim 0.01$. Thus, p-mode periods are affected at the level of only a few percent by the presence of a crystalline lattice. They are therefore of no more interest than are ordinary p-modes in the context of the observed pulsations of the DA and DB variable (DAV and DBV) white dwarfs.

4.2.2. *g-Modes*

We concentrate the remainder of our analysis on the g-modes, since these are the modes that are believed to be responsible for the observed pulsations in the white dwarf variables. Because g-modes have large shears associated with their fluid motions, we expect the nonzero shear modulus μ of the solid to have a significant effect on them. Qualitatively, we may ask when the return force due to a finite shear modulus is approximately equal to the return force normally experienced by fluid elements in the absence of such shear (e.g., Bildsten & Cutler 1995). Algebraically, the shear return force is equal to or exceeds the ordinary return force of the fluid when

$$\frac{\mu}{\rho\sigma^2 h^2} \geq 1 ,$$

where $h \equiv P/|dP/dr|$ is a pressure scale height.

[3] Such short timescale oscillations of tens of seconds may be relevant for accreting white dwarfs in cataclysmic variable systems, although the heating due to accretion may preclude the presence of substantial crystallization in these objects.

In our models, we find that $\mu/(\rho\sigma^2 h^2) > 10^{10}$, which indicates that the g-modes are completely altered in the crystallized region. Thus, a g-mode that is propagating in the fluid region will find a complete mismatch as it attempts to propagate into the crystallized region. We therefore expect nearly complete reflection of the g-mode at such a boundary, with the result that the g-modes are essentially confined to the fluid regions of our models.

5. NUMERICAL ANALYSIS

5.1. *The Global Solution*

We now examine the above assertion and offer a numerical justification for it. Our approach is based on the work of Hansen & Van Horn (1979); we treat the "global" problem, in that we allow the solid cores of our models to respond to the oscillations. We have used the Cowling approximation to simplify the pulsation equations, as was also done in Hansen & Van Horn (1979). Since g-modes in white dwarfs are primarily envelope modes, this is an excellent approximation and hardly affects the accuracy of our calculated periods; even $k = 1$, $l = 2$ modes have periods that are only affected at the level of 0.2% (Montgomery 1998). The details of the rest of the global treatment are summarized in Appendix A, where we describe the oscillation variables, the equations that they obey, the central boundary conditions, and the connecting conditions at the solid/fluid interface.

In Figure 4, we plot the radial and horizontal displacements of a 378.4 s, $l = 1$ mode; the model is again that of a 1.1 $M_\odot$ white dwarf with $T_{\rm eff} = 12{,}200$ K, which is assumed to be 50% crystallized. As is true of all the g-modes we have examined, the amplitude of the fluid motions in the solid is decreased by ~ 3 orders of magnitude compared to that in the fluid. One other feature of the oscillations is that the

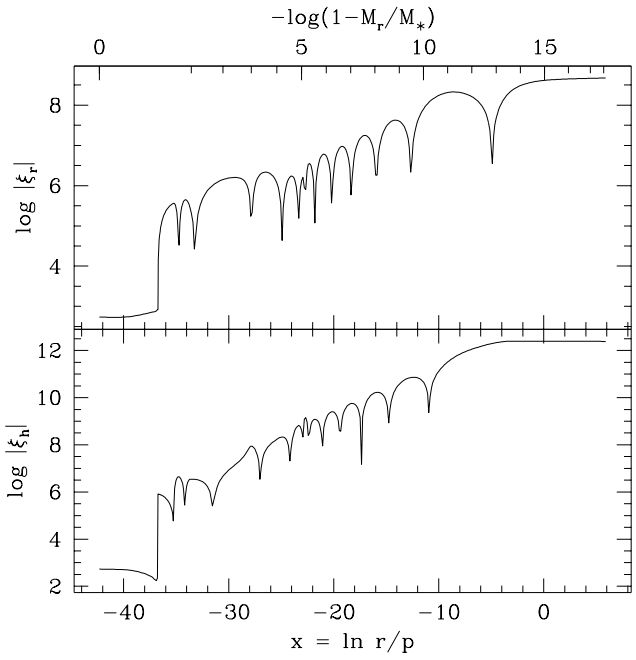

FIG. 4.—Plot of the log of the absolute values of the radial (*top*) and horizontal (*bottom*) displacements as a function of $\ln(r/p)$. Note that ξ_r is continuous at the solid/crystal interface at $\ln(r/p) \sim -36.7$, but ξ_h is not. The magnitudes of both ξ_r and ξ_h are reduced by ~ 3 orders of magnitude as they penetrate the solid region.

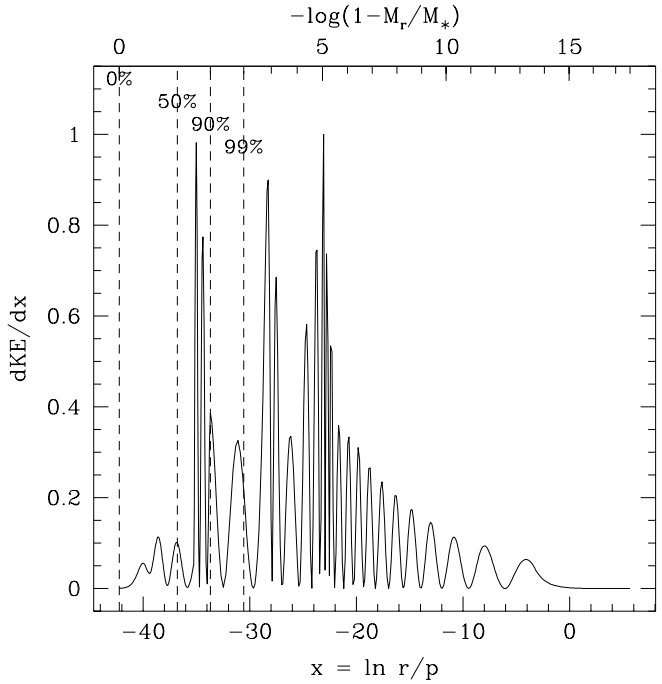

FIG. 5.—Kinetic energy per unit $x = \ln(r/p)$. The vertical dashed lines are labeled with the mass fraction of the model interior to the given point. The mode shown is an $l = 1$, $k = 25$ mode with a period of 673.4 s. The equilibrium model is a 1.1 $M_\odot$ model with $T_{\rm eff}$ at 12,200 K, and the surface layer masses are $M_{\rm He}/M_* = 10^{-3}$ and $M_{\rm H}/M_* = 10^{-5}$.

horizontal displacement is discontinuous at the solid/liquid interface. In the approximation of zero viscosity and laminar flow, the fluid is free to slide over the solid surface. In reality, a turbulent boundary layer would probably form in this region, which would tend to dissipate the pulsation energy.

The kinetic energy density depends on the square of the displacement, so it is attenuated by ~ 6 orders of magnitude in the solid core. Since the kinetic energy is an indicator of how a given mode samples the different regions of a model, we conclude that it is a very good approximation to treat the g-modes as excluded from the solid cores of our models. In the following section we will demonstrate the validity and the self-consistency of this approach.

5.2. *The "Hard-Sphere" Boundary Condition*

As suggested in the previous section, we may be able to reproduce the effects of crystallization on g-mode pulsations merely by applying a hard-sphere boundary condition at the solid/liquid interface. By this we mean that the radial displacement is set to zero ($\xi_r = 0$), and the horizontal displacement is left to be arbitrary. In addition, the boundary condition on the gravitational potential and its derivative are the same as for the uncrystallized case, as we show in Appendix B; these "hard-sphere" calculations are not in Cowling approximation and therefore solve the full fourth-order adiabatic equations in the fluid region. Using the hard-sphere boundary condition has the advantage that the resulting problem is much easier to treat, in terms of both speed and convergence.

We have calculated the fractional difference between periods calculated with the "hard-sphere" approximation and those calculated with the "global" treatment. Using a fiducial model with $M_* = 1.1\ M_\odot$, $T_{\rm eff} = 12{,}200$ K, and assuming 90% crystallization by mass, we have examined all $l = 1$ and 2 periods between 50 and 1000 s. We find that the fractional difference in periods is less than 1 part in 10^4, and that the absolute error in the calculated periods never exceeds 0.05 s. We therefore conclude that the hard-sphere boundary condition at the solid/fluid interface accurately represents the physics of g-mode oscillations in models with crystalline cores. Bildsten & Cutler (1995) found exactly the same approximation to be valid in their treatment of g-modes in the surface oceans of accreting neutron star models.

Before proceeding to the detailed numerical calculations, we wish to convince the reader that crystallization will have a measurable effect on the periods. In Figure 5 we have plotted the kinetic energy per unit $x = \ln(r/p)$, so that the area underneath the curve represents the weight of each region's contribution to the total kinetic energy as a function of x. The vertical dashed lines indicate different mass points in this model. For instance, if the model is 90% crystallized, then the kinetic energy to the left of the 90% line is eliminated from the mode. By visual inspection, this is of the order of 10% of the kinetic energy in the mode, so we might well expect that the period of this mode is affected at the 10% level. In fact, we will see in the next section that the periods can be shifted by even larger amounts.

6. THE g-MODE PERIODS AS A FUNCTION OF $M_{\rm cr}/M_*$

6.1. *Asymptotic Relations*

The kinetic energy argument in § 5.2 leads us to expect that the g-mode periods will change measurably as the crystallized mass fraction increases from 0 to 90%. With this in mind, we reexamine the asymptotic formulae for g-mode periods (e.g., Unno et al. 1989),

$$P_k \sim k\langle \Delta P\rangle\ ,$$

$$\langle \Delta P\rangle = \frac{2\pi^2}{\sqrt{l(l+1)}}\left[\int_{r_1}^{r_2}\frac{N\,dr}{r}\right]^{-1}\ , \qquad (3)$$

where we have written $\langle \Delta P\rangle$ for the mean period spacing between consecutive radial orders. Since the g-modes are excluded from the crystallized region, the inner turning point r_1 is now a function of $M_{\rm cr}/M_*$. Since we allow the model to crystallize while holding all other structural parameters constant, r_1 moves outward, so the integral in equation (3) decreases, with the result that $\langle \Delta P\rangle$ and P_k both increase.

As a heuristic tool, we would like to plot the "region of period formation," which would tell us visually the weight that the different regions of the star have in determining the period of a mode. This problem has been examined several times in the past, for example by Kawaler, Winget, & Hansen (1985), Schwank (1976), Goosens & Smeyers (1974), and originally by Epstein (1950).

To simplify matters, we examine this weight function in the asymptotic limit of high k and l. For g-modes, we must be content to determine a "region of frequency formation." From asymptotic theory, we find that the relative contribution to the total frequency per unit radius is

$$\frac{d\sigma}{dr} \approx \frac{N}{r}\ ,$$

which depends only on N and r. In order to expand the

radial axis in both the center and the envelope, and to make the resulting functions easier to examine, we choose $x = \ln(r/p)$ as our radial coordinate. Then the above relation becomes

$$\frac{d\sigma}{dx} \approx \frac{N}{1+V}\ , \tag{4}$$

where $V \equiv \Gamma_1 gr/c_s^2$. We emphasize that the appearance of the sound speed c_s^2 in the variable V is purely a result of the above radial coordinate change, and does not reflect a dependence of g-mode frequencies on c_s.

In Figure 6, we plot $d\sigma/dx$ versus x for a 1.1 $M_\odot$, $T_{\rm eff}$ = 12,200 K model with $M_{\rm He}/M_* = 10^{-3}$ and $M_{\rm H}/M_* = 10^{-5}$. The three spikes in $d\sigma/dx$ correspond to the composition transition zones of O/C, C/He, and He/H. From inspection of this figure, we would expect the C/He transition zone to have the least effect on the g-mode periods, while the He/H transition zone in the envelope should have the largest effect. Numerically, Bradley (1993) has found this to be the case, with the period spacing and mode trapping being most sensitive to the hydrogen layer mass and least sensitive to the thickness of the helium layer. Physically, this is due to the fact that the He/H transition zone, since it is closest to the surface, is the least degenerate, and so has the largest thermal contributions to the Brunt-Väisälä frequency. In addition, it is the only zone in which there is a contrast in the atomic weight per electron, μ_e. In going from He to H, μ_e goes from 2 to 1; for the O/C and C/He zones, $\mu_e = 2$ for both chemical species in the transition zone.

It is worth commenting on the similarities between the distribution of kinetic energy in Figure 5 and the shape of the g-mode period formation region in Figure 6. The kinetic energy plot is for a numerically calculated $l = 1$, $k = 25$ mode, whereas the period formation region is in the high-k limit. The value of $N/(1+V)$ in Figure 6 should correspond to the wavelength of oscillations as a function of x in Figure 5. This is in fact the case, since we see that peaks in Figure 6 correspond to rapid spatial oscillations in the kinetic energy density. Similarly, the small value of $N/(1+V)$ in Figure 6 for x in the range of -10 to -4 results in a longer spatial wavelength in the oscillations of the kinetic energy density in Figure 5 at this value of x.

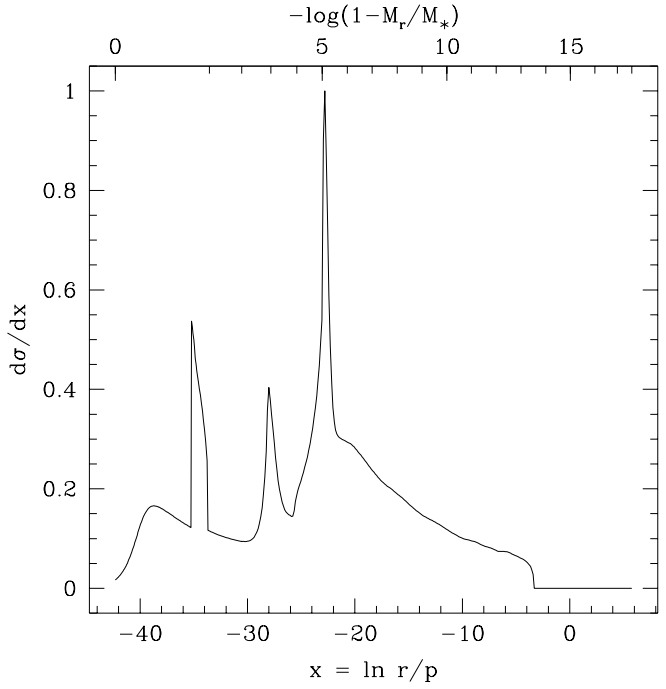

FIG. 6.—Frequency (period) formation region for g-modes in a 1.1 $M_\odot$ model with $T_{\rm eff}$ = 12,200 K. The three spikes are all composition transition zone features, which from left to right are due to the O/C, C/He, and He/H transition zones.

We also note that the overall envelope of the kinetic energy is similar in shape to Figure 6. With this in mind, we calculate the kinetic energy distribution in the asymptotic limit. The kinetic energy, dE, in a shell dr is given by

$$dE \approx \rho r^2\, dr[\xi_r^2 + l(l+1)\xi_h^2]$$
$$\approx \rho r^2\, dr\xi_h^2\ ,$$

where we have used the fact that $\xi_h \gg \xi_r$ for g-modes. If we now substitute for ξ_h the asymptotic value taken from Unno et al. (1989), then we find that the envelope of the kinetic energy density varies as

$$\frac{dE}{dr} \approx \rho r^2 \xi_h^2$$
$$\approx \frac{N}{r}\ . \tag{5}$$

Thus, we see that in the asymptotic limit the kinetic energy samples the model in the same way as does the frequency for g-modes.

Although the above discussion might give the impression that modes of this radial overtone number are safely in the asymptotic limit, such is not the case. For the mode in Figure 5, it can be treated in the asymptotic limit in the region between $x = -20$ and $x = -5$, i.e., its amplitude varies "slowly" compared to the spatial wavelength of the mode. However, the composition transition zone at $x \sim -23$ provides a much more rapid spatial variation than the wavelength of this mode. Depending on the details of how the mode interacts with this feature, it will be partially transmitted and partially reflected at this boundary. Thus, the amplitudes of the mode on each side of a transition zone will not in general be given by the asymptotic theory. In other words, the effect of a transition zone is to enhance the amplitude of a mode on one side of a transition zone relative to its amplitude on the other side. This effect is generically known as "mode trapping," although in the context of white dwarfs this term usually denotes a mode that has an enhanced amplitude in the outer surface layer, i.e., the H layer for DAVs. Returning to the mode in Figure 5, neighboring modes that differ from it by only ± 1 in k still have somewhat different distributions of kinetic energy between the different transition zones. Thus, we cannot consider these modes to be globally described by asymptotic theory.

6.2. *Numerical Results*

We now wish to make a comparison between the functional form of the period spacing implied by equation (3) and that derived from direct numerical calculations. To do this, we normalize $\langle \Delta P \rangle$ to the average period spacing in the uncrystallized case, denoted by $\langle \Delta P \rangle_0$. Such a comparison is shown in Figure 7*a*, where the solid line shows the analytic relation, and the filled circles show the result of a numerical pulsational analysis of $l = 2$ periods between 500 and 1000 s. We have made the model, a 1.1 $M_\odot$ C/O core

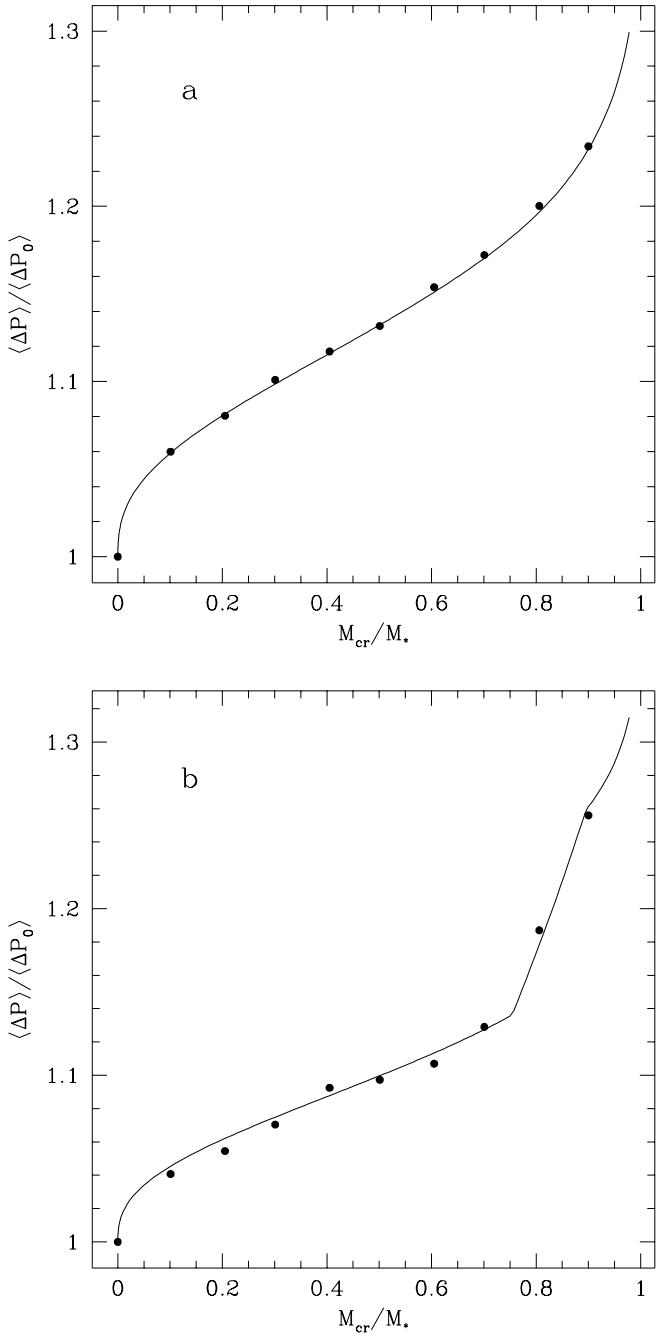

FIG. 7.—Comparison of analytical (*solid line*) and numerical (*filled circles*) period spacings, as a function of M_{cr}/M_*, where each has been normalized to the period spacing in the uncrystallized case. In order to minimize mode trapping effects, the Schwarzschild criterion has been used to compute the Brunt-Väisälä frequency in (*a*), whereas in (*b*) the modified Ledoux prescription has been used. The "kink" in (*b*) for $0.75 \leq M_{cr}/M_* \leq 0.90$ is due to the changing C/O profile in the core.

model with $T_{eff} = 12{,}200$ K, artificially smooth by using the Schwarzschild criterion for the Brunt-Väisälä frequency, which essentially removes the bumps from the Brunt-Väisälä frequency and therefore minimizes mode trapping. The agreement between the two methods is extremely good.

We now examine the more realistic case, where we include the modified Ledoux criterion for the Brunt-Väisälä frequency as described in Brassard et al. (1991). This plot is shown in Figure 7*b*. Although the overall shape of the plot has changed somewhat, the agreement between the asymptotic and numerical results is still quite good. The observed "kink" for $0.75 \leq M_{cr}/M_* \leq 0.90$ is caused by the oxygen mass fraction decreasing from 0.80 to 0.00 in this range. If we examine Figure 6 for the period formation region and we imagine moving the crystallization region to the right, we see that as we encounter the O/C transition zone, the rate of change of the area under the curve doubles, so we would expect the slope of the curve in Figure 7*b* to double as well, which is what we find.

If we use a smaller range of periods to define the period spacing numerically, then we expect mode trapping effects to be amplified even further. This is illustrated in Figure 8, where we have used $l = 2$ periods in the range 500–700 s to calculate a period spacing. Thus, if we have a complete set of observed $l = 2$ periods in this range, we can typically expect "errors" of the order of $\sim 5\%$ in translating this to an asymptotic period spacing.

An equivalent statement to the period spacing increasing with M_{cr}/M_* is that the modes themselves are getting farther apart in period, so that their periods must also be increasing. To illustrate this, we show how a spectrum of mode periods evolves continuously with M_{cr}/M_*. Since mode identification between different models is not a simple matter, we have calculated the spectrum of modes on a fine enough mesh in M_{cr}/M_* so that the period changes are small compared to the differences between consecutive radial overtones. We then identify a given mode at one mesh point with the nearest mode in period of the neighboring mesh point.

The result of this calculation for $l = 2$ periods is shown in Figure 9, where the model considered is a 1.1 $M_\odot$ with $T_{eff} = 11{,}800$ K, $M_{He}/M_* = 10^{-3}$, and $M_H/M_* = 10^{-5}$. We have used the hard-sphere approximation for the solid/liquid boundary and the full Ledoux prescription for the Brunt-Väisälä frequency in calculating these periods. We

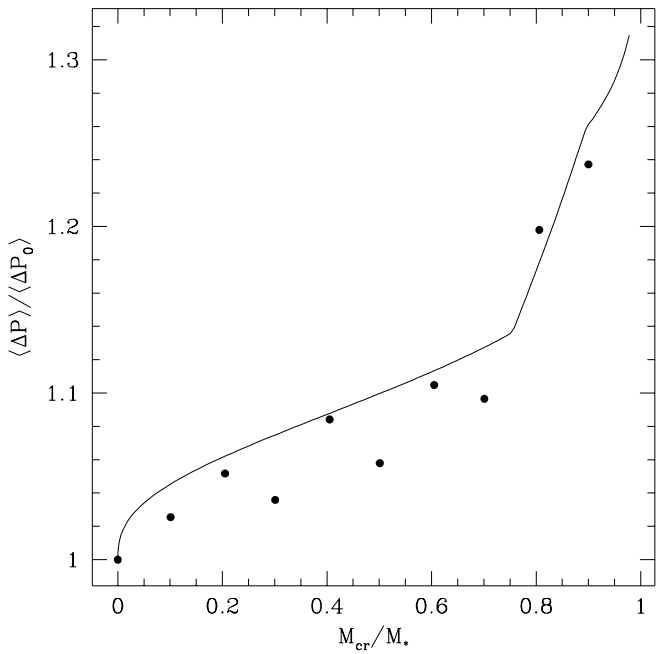

FIG. 8.—Same as Fig. 7*b*, except that periods between 500 and 700 s have been used to define the average period spacing from the pulsation calculations; we have picked this range of periods to mimic that observed in BPM 37093. For this case, we see that mode trapping effects result in larger deviations from the asymptotic relation.

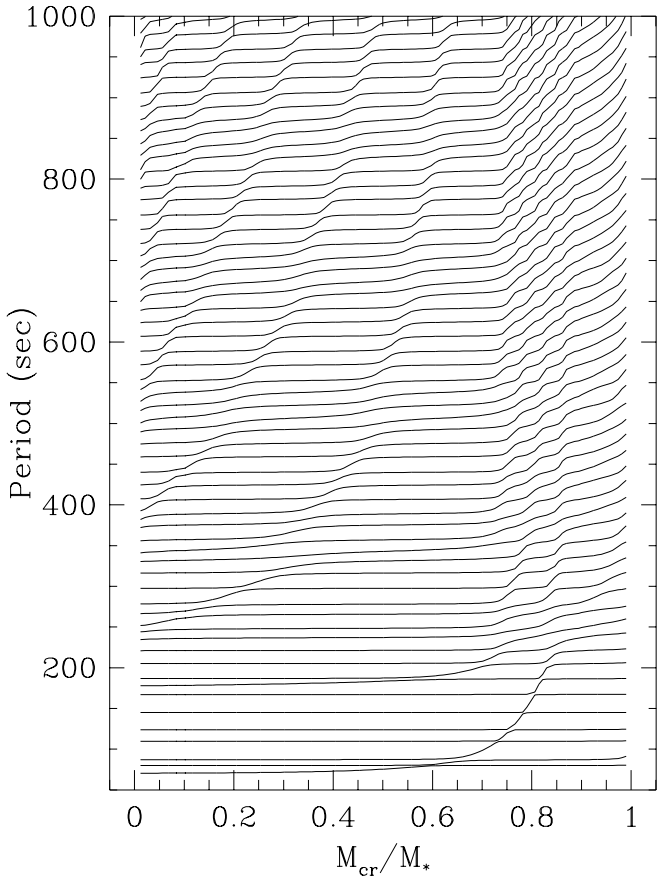

FIG. 9.—Evolution of $l = 2$ g-mode periods as a function of the crystallized mass fraction. We see that in a given region, the periods are either increasing or relatively constant.

have varied the parameter M_{cr}/M_* in increments of 0.01 from 0.00 to 0.99. We note that the periods either appear to be increasing or are relatively constant. In fact, even in regions in which the period of a given mode appears to be constant, its period is still slightly increasing with M_{cr}/M_*.

Figure 9 represents the most detailed calculation to date showing how g-mode periods in white dwarf models evolve as a single parameter is slowly varied (for a previous example, see Wood & Winget 1988). As such, it exhibits many interesting features. First, the "kink" in the periods in the range $0.75 \leq M_{cr}/M_* \leq 0.90$ is again due to the crystallized region moving out into a region with a changing C/O profile; thus, this feature is merely a result of our assumed C/O profile. A more intrinsic feature of this plot are the "avoided crossings." While it is never possible numerically to establish with complete certainty whether or not true avoided crossings occur, the way in which the periods evolve as a function of M_{cr}/M_* is strongly reminiscent of behavior found by Aizenman, Smeyers, & Weigert (1977). For example, the two lowest period modes pictured in Figure 9 have what appears to be an avoided crossing at $M_{cr}/M_* = 0.58$. To the left of this point, the lower period mode has more of its kinetic energy deep in the model near the solid/fluid interface, while to the right of this point it is the higher period mode that has the deeper kinetic energy. Thus, the modes *do* switch character at this point, in the manner found by Aizenman et al. (1977).

Our general result that the g-mode periods increase due to the presence of crystallization is not what was found by Hansen & Van Horn (1979), who reported that the g-mode periods became shorter when the finite shear of the solid core was included. We believe that the resolution of this disagreement lies in a reinterpretation of their calculated periods, not in the periods themselves. Hansen & Van Horn (1979) calculated the periods of $k = 1$ and 2 modes for $l = 1$, 2, and 3, both in the fluid case and in the case of a 99.9% crystallized core. They found that in the crystallized case, the $k = 1$ periods had decreased by approximately a factor of 2 compared to the fluid case; for example, the $l = 1$ period decreased from 193.8 to 99.8 s. Our interpretation is that the 99.8 s mode is actually a new mode, which would not exist if the core were not crystallized. Thus, the main effect of the solid core in their calculations was, in our view, to add an extra mode with a period below that of the previous $k = 1$ mode. To support this, we compare their $k = 1$ periods in the fluid case with their $k = 2$ periods in the solid case. For $l = 1$, 2, and 3, we find that their periods now *increase* from 193.8 to 193.9 s, from 111.9 to 112.0 s, and from 79.1 to 79.2 s, respectively. While these increases are small, they are consistent with what one might expect from a $T_{eff} \sim 10{,}000$ K Fe core white dwarf model that is strongly degenerate in its interior. In addition, the periods in the uncrystallized and the crystallized states are close enough to strengthen our conviction that this is actually the "correct" mode identification.

Using our global code, we are numerically unable to treat models that are more than 97% crystallized. For 97% crystallized models, we do find evidence for low-period "interfacial" modes that do not exist in the uncrystallized case; interfacial modes such as these were found in neutron star models by McDermott et al. (1988). These modes could be the new modes found by Hansen & Van Horn (1979). We caution, however, that we do not understand the properties of these modes, i.e., how they change period as the degree of crystallization changes and whether or not the standard definition of radial overtone number is still meaningful. We are therefore unable to extrapolate these results with confidence to the case of 99.9% crystallization that Hansen & Van Horn treated.

7. $\langle \Delta P \rangle$ AS A FUNCTION OF THE MODEL PARAMETERS

In uncrystallized models, the period spacing is a function of many things, including the total stellar mass, the effective temperature, and the hydrogen layer mass. This is still true in the crystallized case, and we examine the effects that each has on $\langle \Delta P \rangle$. The fiducial model against which we compare our calculations is a model with $M_* = 1.1\ M_\odot$, $T_{eff} =$ 11,800 K, $M_H/M_* = 10^{-5}$, and $M_{He}/M_* = 10^{-3}$. Unless otherwise stated, all periods are calculated using the modified Ledoux prescription for the Brunt-Väisälä frequency.

7.1. *Hydrogen Layer Mass, M_H*

For $0.6\ M_\odot$ models, nuclear burning considerations force M_H/M_* to be smaller than a few times 10^{-4} (Iben & Tutukov 1984; Iben & Macdonald 1985). For models near $1.1\ M_\odot$, this translates into $M_H/M_* \lesssim 10^{-5}$ due to the higher gravities and pressures. We therefore examine models with M_H/M_* between 10^{-10} and 10^{-5}.

In Figure 10*a*, we plot $\langle \Delta P \rangle$ versus log M_H/M_* for different degrees of crystallization, as shown in the legend. For this model, we have used a C/O core and set $M_{He}/M_* = 10^{-3}$ and $T_{eff} = 11{,}800$ K, and we have calculated the Brunt-Väisälä frequency using the Schwarzschild criterion,

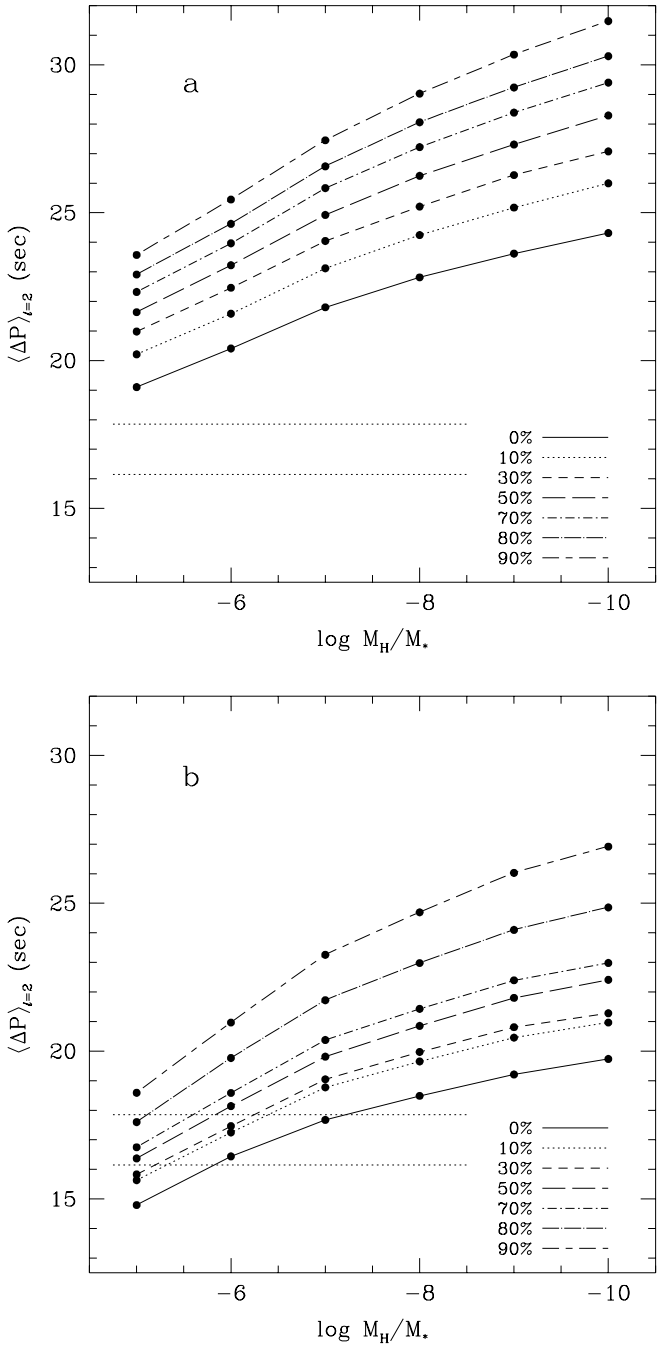

FIG. 10.—(*a*) $\langle \Delta P \rangle$ as a function of log M_H/M_* for differing degrees of crystallization, with N^2 calculated according to the Schwarzschild criterion. (*b*) Same as (a), but with N^2 calculated using the Ledoux prescription.

so that we can minimize mode trapping effects as much as possible. We see that the effect of increasing crystallization is to increase $\langle \Delta P \rangle$ at all compositions. Similarly, the effect of decreasing log M_H/M_* is also to increase $\langle \Delta P \rangle$, for all degrees of crystallization. Thus, a change in one can mimic a change in the other. Figure 10*b* shows the more physical case, where we have used the Ledoux prescription for calculating the Brunt-Väisälä frequency in this model. The same trends are still evident, but the period spacing itself has decreased by 3–4 s for all the models. This difference is due to the nontrivial contribution of the composition transition zones.

The horizontal dashed lines in Figures 10*a* and 10*b* are useful in demonstrating how observations could be used to constrain the parameter space. Here we assume a "measured" value of $\langle \Delta P \rangle \sim 17$ s. The dashed lines represent an uncertainty of 5% in translating this "observed" $\langle \Delta P \rangle$ to an asymptotic value, as is suggested by the deviations due to a finite sampling of the period range in Figure 8. For these calculations, we have calculated the period spacing between consecutive $l = 2$ modes, all with $m = 0$. The exact same dependencies hold for the case of $l = 1$ modes, if the mean period spacings are multiplied by a factor of $\sqrt{3}$.

From Figure 10*b*, we find the following constraints on our parameter space: $-7 \leq \log M_H/M_* \leq -5$ and $0.00 \leq M_{cr}/M_* \leq 0.80$. This is a fairly large range for each parameter, but they are now no longer independent. If we know one of them, then that can reduce the allowed range for the other. For instance, if the model is 50% crystallized, then we must have $-6 < \log M_H/M_* < -5$. From Figure 10*a* we also see that there is no choice of parameters for which the period spacing matches the "observed" value. This demonstrates the large effect that the composition transition zones have on the average period spacing.

7.2. *Total Stellar Mass, M_**

We now consider models that differ only in mass from our fiducial model; all the other parameters are held fixed. In Figure 11*a* we plot the average period spacing for a set of $M_* = 1.15\ M_\odot$ models, again as a function of M_H, where we continue to use the more physical Ledoux prescription for the Brunt-Väisälä frequency. Since the more massive models are smaller in radius, they have a higher average density, and therefore smaller periods and period spacings. For the less massive, $1.05\ M_\odot$ models in Figure 11*b*, we find the opposite is the case; these models are larger in radius and therefore have larger period spacings.

7.3. *Effective Temperature, $T_{\rm eff}$*

In Figure 12 we show how the mean period spacing for $l = 2$ modes varies as a function of the effective temperature of our fiducial models. The horizontal dotted lines again bracket an "observed" period spacing of 17 s. We see that as the models cool, the period spacing increases. This occurs because the models are becoming more degenerate. As the models approach complete degeneracy, the Brunt-Väisälä frequency becomes arbitrarily small, except in composition transition zones, so the periods and period spacings become large.

7.4. *Scaling Relations*

The results of the previous sections can be used to obtain approximate scaling relations for $\langle \Delta P \rangle$. Using models with $T_{\rm eff}$ between 11,200 and 12,800 K, M_* between 1.05 and 1.15 $M_\odot$, and hydrogen layer masses with $H \equiv -\log M_H/M_*$ between 5 and 10 (all ranges inclusive), we obtain the relation

$$\langle \Delta P \rangle_{l=2} = A\bar{f}[1 + 0.54(H - 5)\bar{f}]^{0.24}\bar{M}_*^{-1.7}\bar{T}_{\rm eff}^{-0.95}\ , \quad (6)$$

where $A \equiv 14.7$ s, $\bar{M}_* \equiv M_*/(1.1\ M_\odot)$, $\bar{T}_{\rm eff} \equiv T_{\rm eff}/(12{,}000$ K), and $\bar{f} \equiv \langle \Delta P \rangle / \langle \Delta P \rangle_0$ is the ratio of the asymptotic period spacing at finite crystallization to that at zero crystallization, e.g., the solid line in Figure 7*b*. The bar on f indicates that we have chosen f for an "average" model,

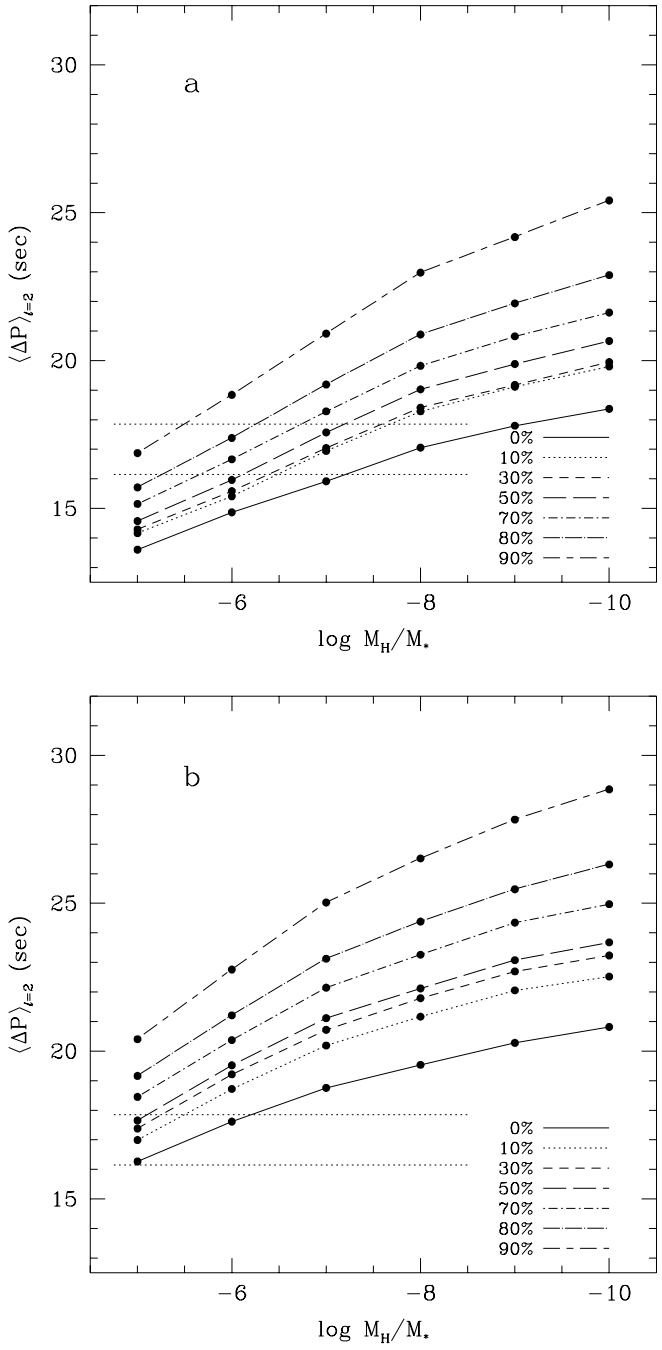

FIG. 11.—Same as Fig. 10*b*, but for (*a*) 1.15 $M_\odot$ and (*b*) 1.05 $M_\odot$ models.

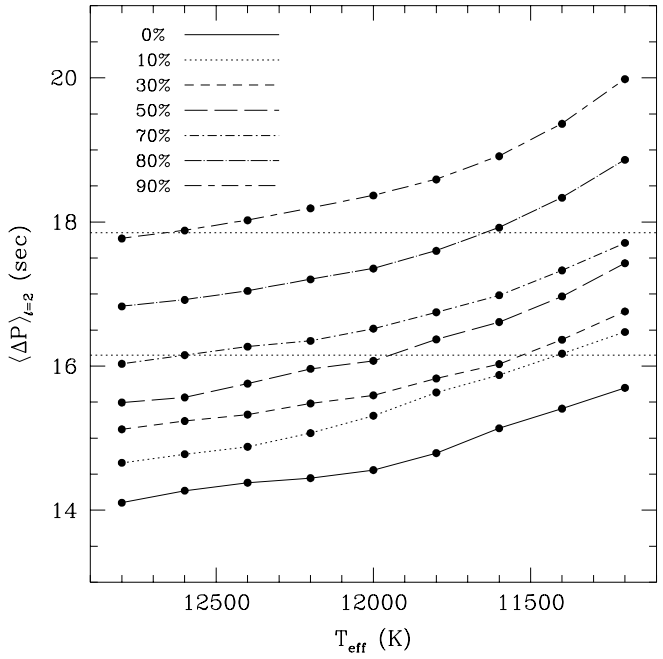

FIG. 12.—Average period spacing as a function of $T_{\rm eff}$ for different degrees of crystallization, as shown in the legend. The models all have $M_* = 1.1\ M_\odot$, $M_{\rm He}/M_* = 10^{-3}$, and $M_{\rm H}/M_* = 10^{-5}$.

where by average we mean a model that has $M_* = 1.1\ M_\odot$, $T_{\rm eff} = 12{,}000$ K, $M_{\rm H}/M_* = 10^{-5}$, and $M_{\rm He}/M_* = 10^{-3}$.

Next, we examine the sensitivity of $\langle \Delta P \rangle$ to small changes in these parameters. If we look at small variations around a model that is 50% crystallized and has an H layer thickness corresponding to $H = 5$, we find

$$\frac{\delta \langle \Delta P \rangle}{\langle \Delta P \rangle} = 0.13\, \delta m_{\rm cr} + 0.15\, \delta H - 1.70\, \frac{\delta M_*}{M_*} - 0.95\, \frac{\delta T_{\rm eff}}{T_{\rm eff}}\,, \tag{7}$$

where we have defined $m_{\rm cr} \equiv M_{\rm cr}/M_*$, and δY represents a small change in a given quantity Y. From fits of spectra of BPM 37093, Bergeron et al. (1995) find $T_{\rm eff} = 11{,}740 \pm 200$ K, and $M_* = 1.09 \pm 0.05\ M_\odot$. From this we see that the errors in the mass determination produce about 5 times the effect of the errors in the temperature determination. Thus, M_* is the most important input parameter that the observations can provide. The quantities $m_{\rm cr}$ and H, the crystallized mass fraction and the negative of the log of the hydrogen layer mass, respectively, are not observable quantities in the standard sense. They can only be determined from an asteroseismological analysis of a particular star, which leads us to the topic of the next section.

8. MODE TRAPPING

The traditional way to obtain information about the surface layer thicknesses of white dwarfs is to use mode trapping information for individual modes, i.e., calculate $\Delta P_k \equiv P_{k+1} - P_k$ directly from the data set and match this to numerical calculations. There is no reason why this will not work now, as long as we have enough well-identified consecutive overtones.

In general, a transition zone may trap a mode in the region above it *or* below it. For a mode to be trapped in the outer hydrogen layer, it needs to have a resonance with the He/H transition region such that its vertical and horizontal displacements both have a node near this interface (Brassard et al. 1992); this is the case that is traditionally referred to as mode trapping in the context of white dwarfs. If we imagine integrating this mode inward from the surface using the boundary conditions there, then we see that all this condition depends on is the mode frequency. Whether or not a frequency that would be trapped is indeed an allowable normal mode frequency *does* depend on the amount of crystallization in the core. From this, we see that it should be possible to disentangle the effects of crystallization and mode trapping.

More precisely, Brassard et al. (1992) find that the average period difference, $\langle \Delta P \rangle_t$, between successively

trapped modes is

$$\langle \Delta P \rangle_t = \frac{2\pi^2}{\sqrt{l(l+1)}} \left(\int_{r_H}^{r_2} \frac{N dr}{r} \right)^{-1}, \quad (8)$$

where r_H is defined as the radius at the base of the hydrogen layer; the integral is therefore over the hydrogen surface layer only. We see that this does not depend on any of the properties of crystallized region, but only on those of the hydrogen envelope.

In Figure 13, we plot the forward period difference, $\Delta P_i \equiv P_{i+1} - P_i$, versus period, P_i, for an equilibrium model with $M_* = 1.1\ M_\odot$, $T_{\rm eff} = 11{,}800$ K, $M_H/M_* = 10^{-5}$, and $M_{He}/M_* = 10^{-3}$. This shows how the mode trapping changes as the crystallized mass fraction is varied from 0.0 to 0.9 in increments of 0.1. In general, we see that the amplitude (strength) of the trapping decreases with increasing crystallization. This is because as the degree of crystallization increases, all modes become more like envelope modes, which decreases the differences between the trapped and untrapped modes.

Concerning the detailed structure of the mode trapping itself, the combined effect of the different transition zones makes it difficult to define a trapping cycle. Furthermore, we see that this structure changes significantly as the degree of crystallization is changed by only 10%. This suggests that we will need to examine the degree of crystallization in smaller increments.

Figure 14*a* is a more detailed version of Figure 13, showing how ΔP changes as the crystallized mass fraction is increased from 0.25 to 0.34 in increments of 0.01. First, we note that there are many trapping features that move uniformly to the right as the degree of crystallization is increased. For instance, there is a trapping feature with a period of $\sim$580 s at 25% crystallization, which migrates to a period range of $\sim$640 s at 32% crystallization. Second, there are many features that remain relatively constant. The

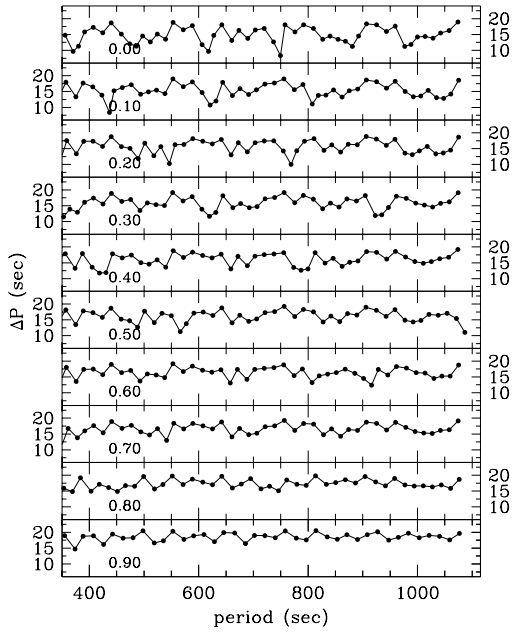

FIG. 13.—$\Delta P_i \equiv P_{i+1} - P_i$ (forward period difference) vs. P_i (period) for $l = 2$ modes. Each panel is labeled by the degree of crystallization assumed for the model, with the other model parameters being held constant.

mode trapping structure in the range 420–500 s is virtually unchanged, and the mode with a period of $\sim$775 s is also somewhat trapped in the majority of the panels. This $\sim$775 s mode has a period that does not evolve as rapidly as many of the other modes. Even so, its period changes by $\sim$0.6 s for every 5% change in the degree of crystallization. Since it is possible to measure periods to quite high accuracies of a few tenths of a second (e.g., Winget et al. 1991, 1994), we should in principle, using modes such as this as well as more sensitive modes, be able to derive quite accurate estimates

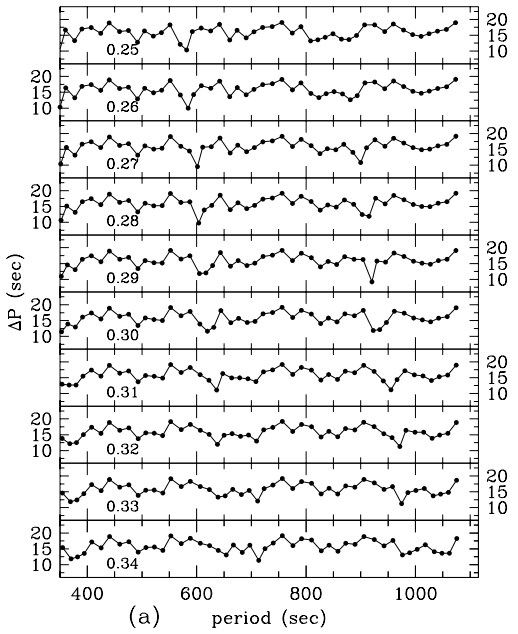

FIG. 14*a*

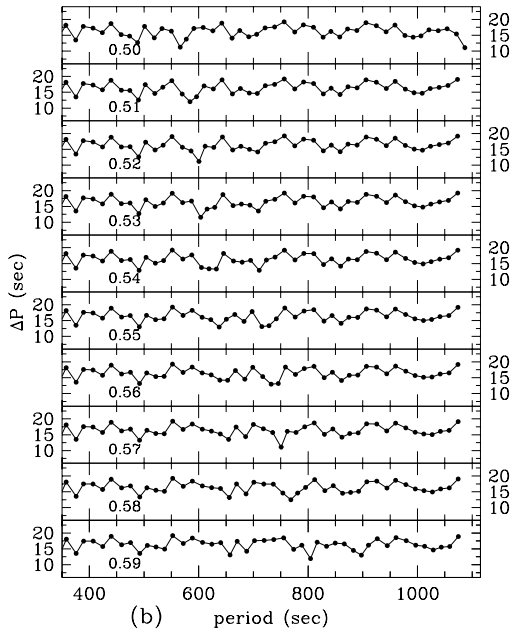

FIG. 14*b*

FIG. 14.—Filled circles connected by lines show the period spacing in the model vs. the period, for degrees of crystallization varying between (*a*) 25% and 34% and (*b*) 50% and 59%.

of the crystallized mass fraction, if we are able to obtain a unique solution.

Figure 14*b* shows a different range of crystallization, this time between 50% and 59%, for the same white dwarf model as used for Figures 13 and 14*a*. Here we see that there is again a trapping feature that migrates through the 600 s region, as well as a mode with a period again at ~ 775 s that tends to be trapped (at least in the upper seven panels). The fact that some periods are strongly affected by changes in the crystallized mass fraction while others are not suggests that we may be able to disentangle the effects of different surface layer masses from those due to crystallization.

9. OBJECTIVE FITTING PROCEDURES

We need an automated procedure for searching parameter space, both to obtain more precise fits and to address the issue of uniqueness of fit. The sensitivity of the trapping features to the crystallized mass fraction is both a blessing and a bane: it is a blessing because this should allow us in principle to determine precise values for $M_{\rm cr}/M_*$, and it is a bane because in practice it requires the computation of an enormous number of models on a fine grid in order to sample the parameter space adequately.

We are currently exploring different methods that would address these issues. The first part of the problem is choosing a method, such as "simulated annealing" or a "genetic algorithm," that can find global minima of multidimensional functions. The second part is automatically generating the equilibrium models with a given set of fit parameters, so that these models can be examined pulsationally. Traditionally, the evolution of such models has been a "hands on" procedure, and this is true of our evolutionary models as well.

Unfortunately, this problem is beyond the scope of this paper. Given the recent increase in both processor speeds and the degree to which problems are being parallelized, it should be possible to implement an objective fitting scheme that will allow us to adequately sample the parameter space of the models. Such an approach is currently being developed at the University of Texas. This should, among other things, allow us to assess objectively the uniqueness of our asteroseismological fits.

10. CONCLUSIONS

In this paper we have calculated the effect of crystallization in the cores of our white dwarf models on the frequency spectrum of pulsations. To a very high degree of accuracy, we find that the kinetic energy of the g-modes is excluded from the crystallized cores of our models. As the degree of crystallization is increased, the kinetic energy of these modes is pushed farther out from the central regions, and both the periods and the mean period spacing, $\langle \Delta P \rangle$, between consecutive radial overtones of the same l increases. Using an "observed" value of $\langle \Delta P \rangle_{l=2} = 17$ s, we show how the range of possible models can be constrained, and how mode-trapping features can be used to obtain more precise information about these fits. Since some periods are strongly affected by changes in the crystallized mass fraction while others are not, we may be able to disentangle the effects of different surface layer masses from those due to crystallization.

The introduction of a crystalline medium that is able to support shear does allow a new class of modes to exist, the torsional or t-modes. Since these modes have zero radial displacement, they should be unable to couple to the overlying fluid layers, and should therefore remain unobservable. The p-modes have periods that are only a few percent different from their uncrystallized values. Since these modes are not observed to be excited, they are also not of interest in the context of BPM 37093 and the other ZZ Ceti's.

By investigating stars such as BPM 37093, asteroseismology may eventually be able to tell us whether crystallization occurs in the way we expect theoretically. Since crystallization and the effects of phase separation are the largest single sources of systematic uncertainties in the white dwarf luminosity function, this would allow us to improve our estimates of the age of the Galactic disk as derived from the observed white dwarf luminosity function. Furthermore, since phase separation, if it occurs, affects the composition of the central regions of white dwarfs, this could systematically affect the observed characteristics of SNe Ia (e.g., total luminosity), which are believed to come from white dwarf progenitors.

Finally, digital surveys now in progress promise to add considerably to the presently known number of cool white dwarfs. For instance, the Sloan Digital Sky Survey (Gunn 1995) should increase this number by a factor of approximately 20, with the result that we may have 20 such stars with which to test the theory of crystallization.

We would like to thank C. J. Hansen for many insights and valuable discussions, as well as the referee for his helpful comments.

This work was supported in part by the National Science Foundation under grant AST 93-15461 and by the NASA Astrophysics Theory Program under grant NAG 5-2818.

APPENDIX A

SPHEROIDAL OSCILLATION EQUATIONS IN A CRYSTALLINE MEDIUM

A1. THE EQUATIONS

We define ξ_r and ξ_h, the radial and horizontal parts of the total displacement, in terms of the total vector displacement, i.e.,

$$\boldsymbol{\xi} = \left[\xi_r(r),\ \xi_h(r) \frac{\partial}{\partial \theta},\ \xi_h(r) \frac{1}{\sin \theta} \frac{\partial}{\partial \phi} \right] Y_l^m(\theta, \phi) . \tag{A1}$$

We take the following equations from Hansen & Van Horn (1979). The oscillation variables are

$$z_1 = \frac{\xi_r}{r},$$

$$z_2 = \frac{1}{\mu_0}\left(\lambda\alpha + 2\mu\,\frac{d\xi_r}{dr}\right),$$

$$z_3 = \frac{\xi_h}{r},$$

and

$$z_4 = \frac{\mu}{\mu_0}\left(\frac{d\xi_h}{dr} - \frac{\xi_h}{r} + \frac{\xi_r}{r}\right),$$

where ξ_r and ξ_h are the radial and horizontal displacements, respectively, as defined in equation (A1), r is the radius, $\lambda = \Gamma_1 p - \frac{2}{3}\mu$, μ is the shear modulus, and $\alpha \equiv (1/r^2)d(r^2\xi_r)/dr - \hat{l}(\xi_h/r)$, with $\hat{l} \equiv l(l+1)$. These variables are the same as those in Hansen & Van Horn (1979) except that we have divided z_2 and z_4 by $\mu_0 \equiv \mu(r=0)$, so that the equations are dimensionless.[4] The fourth-order system of equations (in the Cowling approximation) is then

$$rz_1' = -(1 + 2\lambda\delta)z_1 + \mu_0\,\delta z_2 + \lambda\hat{l}\delta z_3\,, \tag{A2}$$

$$rz_2' = \frac{1}{\mu_0}(-\sigma^2\rho r^2 - 4\rho g r + 4\pi G\rho^2 r^2 + 4\mu\beta\,\delta)z_1 - 4\mu\,\delta z_2 + \frac{\hat{l}}{\mu_0}(\rho g r - 2\mu\beta\delta)z_3 + \hat{l}z_4\,, \tag{A3}$$

$$rz_3' = -z_1 + \frac{\mu_0}{\mu}\,z_4\,, \tag{A4}$$

$$rz_4' = \frac{1}{\mu_0}(g\rho r - 2\mu\beta\delta)z_1 - \lambda\,\delta z_2 + \frac{1}{\mu_0}\{-\rho\sigma^2 r^2 + 2\mu\delta[\lambda(2\hat{l} - 1) + 2\mu(\hat{l} - 1)]\}z_3 - 3z_4\,, \tag{A5}$$

where the prime denotes d/dr, $\delta \equiv (\lambda + 2\mu)^{-1}$, $\beta \equiv 3\lambda + 2\mu$, g is the acceleration due to gravity, and ρ is the density.

A2. CENTRAL BOUNDARY CONDITIONS

Since the models we are considering are crystallized in the center, we need to obtain the boundary conditions in the center, so that we can begin the outward integrations. If we assume that the solutions scale as r^s near the center, we find four solutions: $s = l - 2$, l, $-(l+1)$, and $-(l+3)$. Only the first two solutions are regular at the origin, so they span the space of physical solutions. The general solution near the center is therefore given by

$$\{z_i\} = a\begin{pmatrix} 1 \\ 2(l-1) \\ \dfrac{1}{l} \\ \dfrac{2(l-1)}{l} \end{pmatrix} r^{l-2} + b\begin{pmatrix} \dfrac{(l+1)[\lambda l + \mu(l-2)]}{2[\lambda l(l+2) + \mu(l^2+2l-1)]} \\ \dfrac{(l+1)[\lambda(l^2-l-3) + \mu(l^2-l-2)]}{\lambda l(l+2) + \mu(l^2+2l-1)} \\ \dfrac{\lambda(l+3) + \mu(l+5)}{2[\lambda l(l+2) + \mu(l^2+2l-1)]} \\ 1 \end{pmatrix} r^l\,,$$

where a and b are arbitrary coefficients, and where μ and λ in the above formula are taken to have their central values. These two solutions for the eigenfunction near the center are equivalent to the relations given in Crossley (1975), if the Cowling approximation is used.

A3. THE SOLID/FLUID INTERFACE

In practice, we integrate each independent solution outward from the center. With the exception of z_3, the $\{z_i\}$ are continuous at the solid/fluid interface. Since $z_4 = 0$ in the fluid, we choose the ratio of a and b such that z_4 vanishes at this interface. This leaves only one overall normalization constant. Furthermore, $y_1 = z_1$ at the boundary. Since z_2 is also continuous, we have

$$z_2 = \frac{\lambda\alpha}{\mu_0} = \frac{\lambda V_g(y_1 - y_2)}{\mu_0}\,,$$

[4] We note that there is a typographical error in the definition of z_4 in Hansen & Van Horn 1979 (an additional factor of $1/r$), but it does not propagate throughout the rest of their formulae.

where we have used the oscillation equations in the fluid to express α in terms of the Dziembowski variables $\{y_i\}$. At the fluid/solid interface, if we solve for the $\{y_i\}$ in the fluid in terms of the $\{z_i\}$ in the solid, we find

$$y_1 = z_1 ,$$

$$y_2 = z_1 - \frac{\mu_0}{\lambda V_g} z_2 ,$$

where $V_g = gr/c_s^2$, and λ is now $\Gamma_1 P$, since μ is zero in the fluid. Since we have now specified y_1 and y_2 (up to an overall normalization constant that is present in the $\{z_i\}$), we can now integrate the normal oscillation equations in the fluid (in the Cowling approximation) out to the photosphere of the model.

The main difficulty in applying this procedure is that numerical noise can come to dominate the integrations in the crystalline core. The model that Hansen & Van Horn (1979) considered was a pure Fe core model near 10,000 K. As a result, the theory of crystallization suggested that it should be about 99.9% crystallized by mass. The technique we have used would probably not be viable for this case. The problem is that the two independent solutions, while quite different near the center, become almost linearly dependent farther out. Thus, we lose the ability to calculate the "difference" between the two solutions that is needed in order to set z_4 equal to zero at the solid/fluid interface. For our program, numerical noise dominates this process for g-modes in models that are more than 98% crystallized.

In terms of the physics, however, we are somewhat overdramatizing the situation, since nearly all of the pulsational results in this paper are based on the simple approximation that $y_1 = 0$ at the solid/fluid boundary. From the self-consistent treatment, we have found this to be an extremely good approximation from 0% crystallization to 98% crystallization, and we have no reason to believe that this situation will change at higher amounts of crystallization. Using this simplified treatment ($y_1 = 0$ at the solid/fluid boundary), we are therefore able to treat accurately arbitrary degrees of crystallization.

APPENDIX B

THE BOUNDARY CONDITIONS ON $\Phi'(r)$ AT THE CRYSTALLIZATION BOUNDARY

The perturbations to the gravitational potential are, of course, generated by the perturbations in the density. They can therefore be written as

$$\Phi'(\boldsymbol{r}) = G \int dV' \, \frac{\rho'(\boldsymbol{r}')}{|\boldsymbol{r} - \boldsymbol{r}'|} , \tag{B1}$$

where we have assumed that the density vanishes at the surface. If we now write $\Phi'(\boldsymbol{r}) = \Phi'(r) Y_l^m(\theta, \phi)$ and $\rho'(\boldsymbol{r}') = \rho'(r') Y_l^m(\theta', \phi')$ and use the usual expansion of $|\boldsymbol{r} - \boldsymbol{r}'|$ in surface harmonics, then we arrive at the result of Christensen-Dalsgaard (1976),

$$\Phi'(r) = \frac{4\pi G}{2l+1} \left[r^{-(l+1)} \int_0^r \rho'(r') r'^{l+2} \, dr' + r^l \int_r^R \rho'(r') r'^{-l+1} \, dr' \right] . \tag{B2}$$

We will assume that there is no motion for $r < r_x$, where r_x is the radius of the crystallization boundary. Thus, we have $\rho'(r) = 0$ for $r < r_x$. If we now take a derivative of $\Phi'(r)$ in the region $r_x < r < R$, we find

$$\frac{d\Phi'(r)}{dr} = \frac{4\pi G}{2l+1} \left[-(l+1) r^{-(l+2)} \int_0^r \rho'(r') r'^{l+2} \, dr' + l r^{l-1} \int_r^R \rho'(r') r'^{-l+1} \, dr' + r\rho'(r) - r\rho'(r) \right] ,$$

where we have assumed that the density is zero at the outer boundary. Evaluating this at $r = r_x$, and remembering that $\rho'(r) = 0$ for $r < r_x$, we find that the first integral vanishes, which, along with the cancellation of the last two terms, leaves only

$$\frac{d\Phi'(r_x)}{dr} = \frac{4\pi G}{2l+1} \, l r_x^{l-1} \int_{r_x}^R \rho'(r') r'^{-l+1} \, dr' . \tag{B3}$$

Finally, using equation (B2) to evaluate $\Phi'(r)$ at $r = r_x$, and combining it with equation (B3), we obtain the final result:

$$\frac{d\Phi'(r_x)}{dr} = \frac{l}{r_x} \Phi'(r_x) . \tag{B4}$$

This is the same boundary condition as usually encountered in the uncrystallized case for r approaching zero (see, e.g., Unno et al. 1989); we see that it is unchanged by the presence of a rigid, crystallized core.

APPENDIX C

GLOBAL CONSERVATION OF MOMENTUM FOR $l = 1$ MODES

As a final note, we mention that the derivation by Christensen-Dalsgaard (1976) that $l = 1$ modes conserve the total

momentum of the system and are therefore allowable pulsation modes is easily extended to the present case, in which we have a solid, completely rigid core, surrounded by a fluid envelope in which there are pulsations.

In the present case, the center of mass of the fluid in the envelope *is* displaced by the pulsations. However, the pressure variations associated with these pulsations in the fluid exert a net force on the crystalline core, causing its center of mass to move also. Considered as a system, the core plus envelope conserves momentum, so that there is no net displacement of the center of mass, and $l = 1$ oscillations are again allowed.

REFERENCES

Abrikosov, A. A. 1960, Zh. Eksp. Teor. Fiz., 39, 1798
Aizenman, M., Smeyers, P., & Weigert, A. 1977, A&A, 58, 41
Alterman, Z., Jarosch, H., & Pekeris, C. L. 1959, Proc. R. Soc. London A, 252, 80
Arcoragi, J. P., & Fontaine, G. 1980, ApJ, 242, 1208
Bergeron, P., Wesemael, F., Lamontagne, R., Fontaine, G., Saffer, R. A., & Allard, N. F. 1995, ApJ, 449, 258
Bildsten, L., & Cutler, C. 1995, ApJ, 449, 800
Bradley, P. A. 1993, Ph.D. thesis, Univ. Texas at Austin
Bradley, P. A., Winget, D. E., & Wood, M. A. 1993, ApJ, 406, 661
Brassard, P., Fontaine, G., Wesemael, F., & Hansen, C. J. 1992, ApJS, 80, 369
Brassard, P., Fontaine, G., Wesemael, F., Kawaler, S. D., & Tassoul, M. 1991, ApJ, 367, 601
Christensen-Dalsgaard, J. 1976, MNRAS, 174, 87
Crossley, D. J. 1975, Geophys. J. RAS, 41, 153
Epstein, I. 1950, ApJ, 112, 6
Fontaine, G., Graboske, H. C., Jr., & Van Horn, H. M. 1977, ApJS, 35, 293
Garnavich, P. M., et al. 1998, ApJ, 493, L53
Goosens, M., & Smeyers, P. 1974, Ap&SS, 26, 137
Gunn, J. E. 1995, BAAS, 186, 4405
Hansen, C. J., & Van Horn, H. M. 1979, ApJ, 233, 253
Höflich, P., Wheeler, J. C., & Thielemann, F. K. 1998, ApJ, 495, 617
Iben, I. J. 1991, ApJS, 76, 55
Iben, I. J., & Macdonald, J. 1985, ApJ, 296, 540
Iben, I. J., & Tutukov, A. V. 1984, ApJ, 282, 615
Kanaan, A. N. 1996, Ph.D. thesis, Univ. Texas at Austin
Kanaan, A., Kepler, S. O., Giovannini, O., & Diaz, M. 1992, ApJ, 390, L89
Kawaler, S. D., Winget, D. E., & Hansen, C. J. 1985, ApJ, 295, 547
Kirzhnits, D. A. 1960, Soviet Phys.—JETP, 11, 365
Lamb, D. Q. 1974, Ph.D. thesis, Univ. Rochester
Lamb, D. Q., & Van Horn, H. M. 1975, ApJ, 200, 306
Landau, L. D., & Lifshitz, E. M. 1975, Theory of Elasticity (Oxford: Pergamon)
McDermott, P. N., Van Horn, H. M., & Hansen, C. J. 1988, ApJ, 325, 725
Montgomery, M. H. 1998, Ph.D. thesis, Univ. Texas at Austin
Ogata, S., & Ichimaru, S. 1987, Phys. Rev. A, 42, 5451
Salpeter, E. 1961, ApJ, 134, 669
Schwank, D. C. 1976, Ap&SS, 43, 459
Unno, W., Osaki, Y., Ando, H., Saio, H., & Shibihashi, H. 1989, Nonradial Oscillations of Stars (Tokyo: Univ. Tokyo Press)
Van Horn, H. M., & Savedoff, M. P. 1976, In Proc. Solar and Stellar Pulsation Conference, ed. A. N. Cox & R. G. Deupree (LASL Rept. LA-6544-C; Los Alamos: Los Alamos Scientific Laboratory), 109
Winget, D. E., Kepler, S. O., Kanaan, A., Montgomery, M. H., & Giovannini, O. 1997, ApJ, 487, L191
Winget, D. E., et al. 1991, ApJ, 378, 326
———. 1994, ApJ, 430, 839
Wood, M. A. 1990, Ph.D. thesis, Univ. Texas at Austin
———. 1992, ApJ, 386, 539
Wood, M. A., & Winget, D. E. 1988, In Proc. Multimode Stellar Pulsations Workshop, ed. G. Kovács, L. Szabados, & B. Szeidl (Budapest: Konkoly Obs.), 199